Materials Characterization 199 (2023) 112764

Contents lists available at ScienceDirect

Materials Characterization

journal homepage: www.elsevier.com/locate/matchar

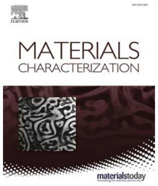

# Effect of evolution of spinodal decomposition on microstructure and properties in multi-step aged FeCrCo alloy

Zhaolong Xiang [a,b,c], Lin Zhang [a], Bailing An [a,b], Jun Lu [b], Rongmei Niu [b], Yan Xin [b], Masoud Mardani [b], Theo Siegrist [b], Robert E. Goddard [b], Tiannan Man [a], Tao Wang [a], Engang Wang [a,*], Ke Han [b,*]

[a] *Key Laboratory of Electromagnetic Processing of Materials (Ministry of Education), Northeastern University, Shenyang 110819, China*
[b] *National High Magnetic Field Laboratory, Florida State University, Tallahassee 32310, FL, USA*
[c] *Shanghai Key Lab of Advanced High-temperature Materials and Precision Forming, Shanghai Jiao Tong University, Shanghai 200240, China*

## ARTICLE INFO

*Keywords:*
FeCrCo alloys
Spinodal decomposition
Step aging
STEM
Magnetic properties
Hardness

## ABSTRACT

Although much effort has been devoted to the study of the relationship between properties and modulated structure in FeCrCo alloys, the connection between their structure and composition at atomic scale and their magnetic and mechanical properties at macroscale remains largely unclear. We explored this connection by tracing the evolution of microstructure and composition in FeCrCo (using data from STEM-HAADF/EDS) and correlating this evolution to the development of magnetic and mechanical properties during the step aging process. The results indicated that, during the decomposition of $\alpha$ into $\alpha_1$ and $\alpha_2$, the size of the $\alpha_1$ phase increased (from 10 to 36 nm) as step aging progressed. The volume fraction of the $\alpha_1$ phase increased in early stages of spinodal decomposition, then remained unchanged in later stages. The $\alpha_1$ phase was rich in Fe and Co. By contrast, the $\alpha_2$ phase was rich in Cr. The composition difference between $\alpha_1$ and $\alpha_2$ increased during the first six stages but decreased in the last stage. A close examination of the atomic structure showed that the lattice misfit increased as step aging progressed. Both magnetic and hardness properties increased as step aging progressed, but remanence and hardness decreased slightly in the final stage.

## 1. Introduction

FeCrCo permanent magnet alloys were introduced in the 1970s [1,2]. They have attracted a great deal of attention because of their excellent machinability [2,3] far superior to the AlNiCo5 alloys that are often used in similar applications [4,5]. FeCrCo can be formed into thin wires or sheets for applications in such devices as electric motors [6], telephone receivers [7,8], printers, stereo-cartridges, and so on [9]. Because of their high Curie temperature (650 °C) [10,11] and high corrosion resistance [12], FeCrCo functions well at high temperatures and in harsh environments [13].

Although the magnetic properties of FeCrCo are not as good as those of NdFeB [14–16], FeCrCo preserves its magnetic strength at high temperatures (up to 400 °C) where NdFeB loses almost all magnetic properties [17]. In comparison with SmCo, which is known for high thermal stability [18,19], FeCrCo falls short in magnetic properties but preserves its high ductility [20].

The FeCrCo phase diagram shows five solid phases ($\alpha$, $\gamma$, $\sigma$, $\alpha_1$, $\alpha_2$) [21–23]. Both the $\gamma$ phase and $\sigma$ phase are adverse to magnetic properties, and the $\sigma$ phase is also adverse to mechanical properties [11]. A miscibility gap in the FeCrCo system was identified by Kaneko et al., who used measurements of mechanical hardness and Curie temperature [23]. Hasebe et al. computed the miscibility gap of $\alpha$-Fe-X systems by measuring magnetic effects in samples subjected to thermodynamic treatments [24]. Minowa et al. further studied the shape of the miscibility gap in FeCrCo alloys by using a transmission electron microscope (TEM) and by monitoring changes in magnetic properties [25].

Magnetic and mechanical properties in FeCrCo alloys result from spinodal decomposition, which occurs within the miscibility gap [26,27]. Spinodal decomposition results when the high-temperature $\alpha$ phase decomposes into a modulated structure consisting of two lower-temperature phases: $\alpha_1$ (a strongly ferromagnetic, iron and cobalt-rich phase) and $\alpha_2$ (a weakly ferromagnetic, chromium-rich phase) [28,29].

Previous studies showed that the desirable magnetic properties of

---

* Corresponding authors.
*E-mail addresses:* egwang@mail.neu.edu.cn (E. Wang), han@magnet.fsu.edu (K. Han).

https://doi.org/10.1016/j.matchar.2023.112764
Received 4 December 2022; Received in revised form 14 February 2023; Accepted 24 February 2023

FeCrCo alloys were closely related to the shape and arrangement of the nanosized $\alpha_1$ particles [30]. Several research groups have subjected the alloys to external magnetic fields [13,31,32] and to mechanical deformation [33–35] in order to induce the $\alpha_1$ phase to elongate and line up parallel to the direction of the magnetic field or of the deformation. The result was that magnetic properties were enhanced.

Step aging is an efficient method to achieve desired $\alpha_1$ phase and magnetic properties. The aging starts at relatively high temperature (at about 645 °C) in order to accelerate the initiation of decomposition because the substitutional elements need high temperature for diffusion. The solubility of the alloying elements at this temperature, however, is high, leading to the decomposed phases have relatively small composition difference and therefore weak magnetic properties. One therefore must gradually decrease the temperature in order to decrease the solubility of the alloying elements in order to increase the composition differences of Fe, Cr and Co elements between the two phases. The temperature must be decreased gradually to keep sufficient diffusion rate. To compensate for the decrease in diffusion rate, one has to increase the aging time when decreasing temperature. When the temperature gradually decreases to a lowest temperature for practical applications (at about 520 °C), the enrichment degree of Fe, Cr and Co elements between the two phases should reach the maximum, leading to that the composition difference between the two phases reaches the maximum and magnetic properties reach the optimized value. Other studies have shown that differences in magnetic properties are related to the variations in the process of step aging [32,36]. These variations affect the size, volume fraction, and composition of the $\alpha_1$ and $\alpha_2$ phases. Mössbauer spectrometry has been used to investigate phase composition in order to clarify its effect on magnetic properties [37–39], but this technique cannot quantify size, volume fraction, and composition at the same time. To resolve this problem, we used atomic resolution high-angle-annular-dark-field scanning transmission electron microscopy (HAADF-STEM) [40].

The application of FeCrCo alloys is affected not only by magnetic properties but also by mechanical properties [26,41]. Several research groups have reported strength enhancement as a result of spinodal decomposition, but the hardening mechanism of FeCrCo still needs study [42,43]. It is generally accepted that hardness enhancement also results from spinodal decomposition. When lattice mismatch occurs during decomposition, it generates internal stress, thus blocking dislocation motions. In our previous research, we discussed the effect on hardness brought about by composition fluctuations that occurred in a later stage of the spinodal decomposition of an FeCrCo alloy placed under a magnetic field [40].

In this study, Fe58Cr27Co15 samples were prepared by electric arc furnace melting. These samples were subjected to solution treatment, then aged in seven steps. Using HAADF-STEM, we studied the evolution of the microstructure and composition of various phases formed during the spinodal decomposition that occurred during the step aging of Fe58Cr27Co15 samples. We further compared the sizes, volumes, and compositions of the $\alpha_1$ and $\alpha_2$ phases to establish parameters that could then be correlated with the changes in magnetic properties resulting from each of the seven stages of step aging. We also measured the wavelength and amplitude of decomposition at each stage, as well as the lattice misfit between the $\alpha_1$ and $\alpha_2$ phases. These parameters were used to analyze hardness evolution during step aging and deduce the mechanism for enhancement of desirable properties.

## 2. Experimental procedures

The Fe58wt%Cr27wt%Co15wt% ingot used in this study was prepared with oxygen-free Fe (99.99 wt%), high-purity Co (99.95 wt%), and high-purity Cr (99.96 wt%) in a vacuum electric arc furnace in a hemispherical copper mold with an inner diameter of 40 mm. This ingot was placed in the center of a high-temperature resistance furnace under high-purity Ar atmosphere for two hours of solution treatment at 1300 °C (Fig. 1), after which it was cut into eight samples (ST, SA1, SA2, SA3, SA4, SA5, SA6, and SA7, each measuring 10 × 10 × 15 mm$^3$). Sample ST was set aside and received no further step aging. The other seven samples were moved to a low-temperature resistance furnace under high-purity Ar atmosphere for further step aging. Step 1 aging treatment was done at 645 °C for 10 min for sample SA1, Step 2 (at 645 °C for 1 h) for sample SA2, Step 3 (combining Step 2 treatment with additional treatment at 620 °C for 1 h) for sample SA3, Step 4 (combining Step 3 treatment with additional treatment at 600 °C for 2 h) for sample SA4, Step 5 (combining Step 4 treatment with additional treatment at 580 °C for 3 h) for sample SA5, Step 6 (combining Step 5 treatment with additional treatment at 560 °C for 4 h) for sample SA6, Step 7 (combining Step 6 treatment with treatment at 540 °C for 5 h, followed by further treatment at 520 °C for 6 h) for sample SA7 (Fig. 1). After step aging, samples SA1-SA7 were air-cooled to room temperature.

All eight samples were polished and examined by X-ray diffraction to determine peak shift in a Scintag X-ray diffractometer with a scintillator detector and graphite-monochromated Cu Kα radiation (wavelength λ 1.5406 Å). In order to accurately analyze the peak shift in the (110), (200), and (211) directions, the scanning angle was set to move in one-second steps of 0.0025° and collected data from 43° to 46°, 63° to 66°, and 81° to 85°. We used NIST standard Si powder to correct instrument effect.

From each step-aged sample, we sliced thin specimen sheets (each 10 × 15 × 0.5 mm$^3$) to be prepared for later Scanning Transmission Electron Microscopy (STEM) examination. These specimens were ground to a thickness of 30 μm. From each, a 3 mm diameter disk was punched out and ion-milled at 3–5 keV with an incidence angle of 7°. We acquired high angular annual dark field (HAADF) STEM images using a probe-aberration-corrected, cold-field-emission JEM JEOL-ARM200cF equipped with a JEOL HAADF-STEM detector, operating at 200 kV. These images were taken with a 40 μm condense lens aperture with a medium spot size (4c in our ARM200cF) at an image scan speed of 32 pixels/μs. The beam convergence angle was 21 mrad [44–46]. We used the Oxford Aztec system of Energy Dispersive Spectroscopy (EDS) to obtain EDS Spectrum Imaging (EDS-SI) for our analyses of the changes in elemental composition in the $\alpha_1$ and $\alpha_2$ phases of the specimens.

Vickers hardness tests were performed using a diamond indenter under a load of 500 g with a dwelling time of 10 s. From each of the step-aged samples, we prepared an additional specimen (3 mm in diameter, 10–20 μm thick) for examination at a temperature of 298 K of the hysteresis loops of these specimens. For this examination, we used the Vibrating Sample Magnetometer (VSM) installed in a Physical Property Measurement System (PPMS) made by Quantum Design Inc., which has a maximum applied field of 9 T.

## 3. Results

### 3.1. Magnetic properties and hardness

Vickers hardness tests of samples (ST and SA1-SA7) showed that hardness values gradually increased from sample SA1 (i.e. step 1) to sample SA6 (i.e. step 6) but stopped this trend from sample SA6 to sample SA7 (i.e. step 7) (Fig. 2). This trend was consistent with the chemistry fluctuation amplitude of Cr and Co (see Section 3.4). Hardness values increased by 6.4% from sample SA1 to sample SA2, 1.9% from sample SA2 to sample SA3, 17.4% from sample SA3 to sample SA4, 12.9% from sample SA4 to sample SA5, and 14.5% from sample SA5 to sample SA6. The largest increase in both hardness value and composition amplitude occurred from sample SA3 to sample SA4 (Cf. Figs. 12 and 2). From sample SA6 to sample SA7, however, hardness values decreased marginally by 0.98%. This decrease in hardness may reflect a decrease in the amplitude of Cr and Co, combined with an increase in the wavelength of spinodal decomposition (see Section 4.1).

The hysteresis loops of the step-aged samples SA1-SA7 showed that the values of both remanence and coercivity gradually increased with

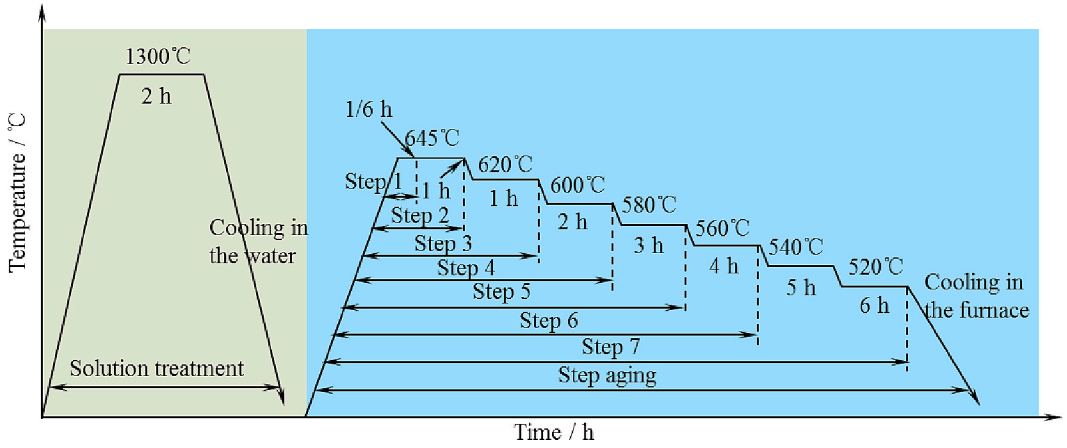

**Fig. 1.** Schematics of solution treatment and step aging of FeCrCo samples.

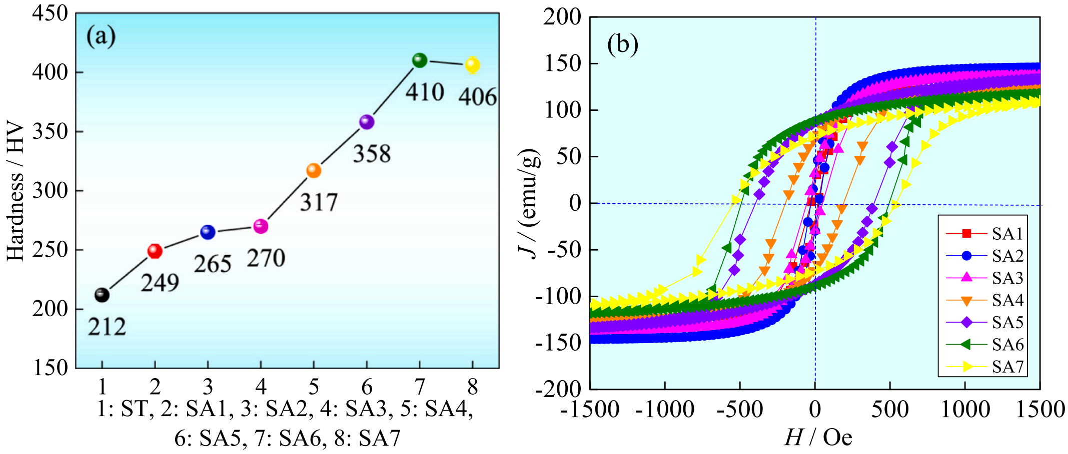

**Fig. 2.** Vickers hardness and hysteresis loops of sample ST (no step aging), sample SA1 (step 1), sample SA2 (step 2), sample SA3 (step 3), sample SA4 (step 4), sample SA5 (step 5), sample SA6 (step 6), and sample SA7 (step 7). (a) Vickers hardness. Some error bars are too small to show in the Figure. Vickers hardness of solution treated samples after step aging increased by 17.4%, 25.0%, 27.4%, 49.5%, 68.9%, 93.4%, and 91.5%, respectively for samples SA1-SA7. (b) Hysteresis loops.

further step aging from sample SA1 to sample SA6. From sample SA6 to sample SA7, coercivity increased, but remanence decreased. This divergence between the two trend lines may be related to a shift in the relative compositions, sizes, and volume fractions of the $\alpha_1$ and $\alpha_2$ phases. From sample SA1 to sample SA2, coercivity increased by 3.8% and remanence by 31.9%; from sample SA2 to sample SA3, coercivity increased by 96.3% and remanence by 14.0%; from sample SA3 to sample SA4, coercivity increased by 258.5% and remanence by 113.8%; from sample SA4 to sample SA5, coercivity increased by 106.8% and remanence by 25.3%; from sample SA5 to sample SA6, coercivity increased by 25.4% and remanence by 3.2%; and from sample SA6 to sample SA7, coercivity increased by 9.9%, but remanence decreased by 19.1%. The increase in both coercivity and remanence from sample SA3 to sample SA4 was larger than the others (Fig. 2b). This corresponds to changes resulting from step aging times (see Section 4.2).

### 3.2. Analysis of X-ray diffraction

All of the samples were subjected to XRD testing, including sample ST (which was solution treated but not step-aged), and samples SA1-SA7 (which were both solution treated and step-aged). We used a finer step size (0.0025°) to study the changes that occurred during step aging in lattice constants. The crystal phase identified is the bcc-α phase. For the (110), (200), and (211) reflections, the peaks for samples SA1-SA7 showed a downward shift compared to those for sample ST. In the step-aged samples SA1-SA7, the downward shift of the peaks increased as step aging progressed (Fig. 3a-c). When we calculated average lattice constants using the (110), (200), and (211) reflections, we found that 1) the constants of all the step-aged samples were larger than the constant of the non-step-aged sample, and 2) they all increased as step aging progressed (Fig. 3d).

Although XRD revealed that the peak shifts were the results of decomposition, it could not distinctly separate the $\alpha_1$ phase from the $\alpha_2$ phase, both of which had same crystallographic structure as the mother α phase. We thus used STEM/EDS to do further analysis on the assumption that the major difference between the $\alpha_1$ and $\alpha_2$ was chemical composition rather than crystalline structure.

### 3.3. Analysis of evolution of structure

Using conventional TEM, previous researchers have confirmed the presence of $\alpha_1$ and $\alpha_2$ phases in the late stage of spinodal decomposition in FeCrCo [20,47]. So far, however, neither Selected-Area Diffraction Patterns (SADPs) of the crystal structure nor HAADF-STEM imaging for the atomic structure have been reported for early stages of decomposition of this alloy.

It is well known that spinodal decomposition occurs only in unstable regions. Such a region appears in phase diagrams as a miscibility gap.

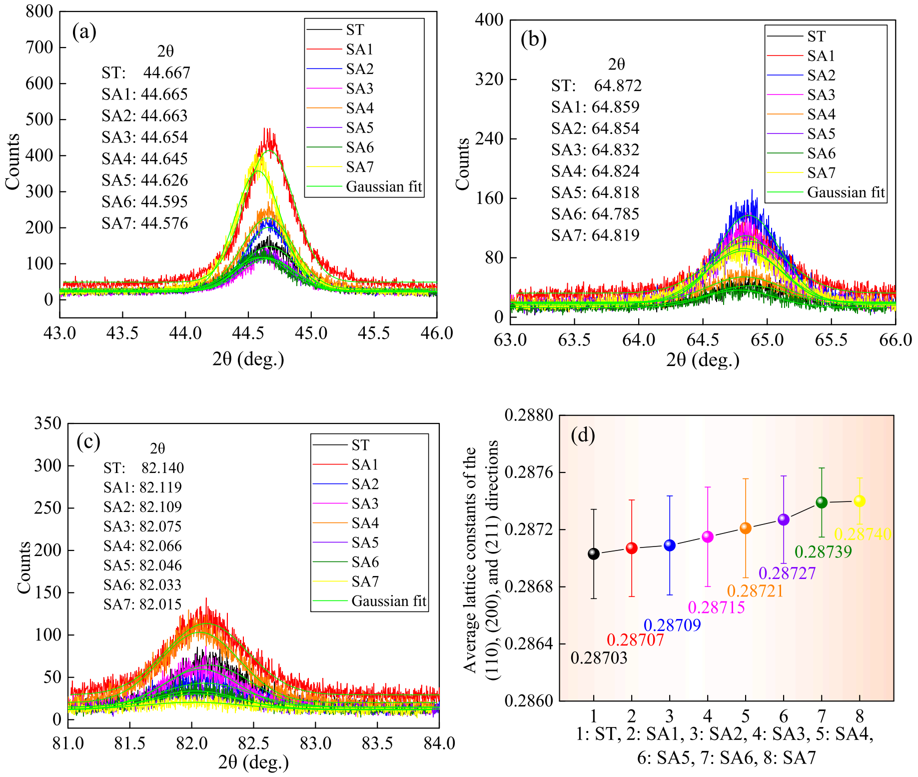

**Fig. 3.** X-ray diffraction patterns and average lattice constants of sample ST and samples SA1-SA7 from various scanning angles. (a) 43–46°. (b) 63–66°. (c) 81–84°. (d) Average lattice constants calculated using the Bragg reflection angles (2θ) of (110), (200), and (211) from samples ST and SA1-SA7. We used Gaussian fit in Origin to get 2θ value.

When certain alloys are heated, phase separation occurs spontaneously in the miscibility gap without any nucleation process. Consequently, spinodal decomposition will require less time. In our previous studies, we found that the SADPs of FeCrCo were ellipsoid in the later stage of spinodal decomposition [40]. Other researchers have described ellipsoid SADPs that appeared during the initial stages of FeC martensite decomposition [48]. Similar ellipsoid diffraction spots have also been reported in Cu15Ni8Sn alloys [49,50]. In this study, during the initial aging of FeCrCo, we found not only similarly ellipsoid SADPs but also two diffraction spots at (110) and (200) (Fig. 4b). The presence of ellipsoid SADPs indicates that a modulated microstructure (i.e., one with both $\alpha_1$ and $\alpha_2$ phases) had occurred despite the fact that the sample had been annealed at 645 °C for only 10 min.

Using TEM, prior researchers have observed periodic structure in CuNiCr alloys during the initial stages of aging, indicating that spinodal decomposition had occurred [51]. We did not, however, observe a clear periodic structure in sample SA1 (step 1: 645 °C for 10 min), using either TEM or low magnification HAADF-STEM (Fig. 4a and c). At the atomic scale, however, we observed that some regions appeared darker than others (Fig. 4d). The bright-dark contrast between neighboring regions reflects a change in intensity that is proportional to the square of the atomic numbers of the atoms in the two neighboring regions [52,53]. Since the atomic number of Cr (24) is smaller than that of either Fe (26) or Co (27), we deduced that the dark regions were rich in Cr and the bright regions were rich in Fe and/or Co. When we drew a profile line from a dark region to a bright region, we found that the intensity ratio of each atom increased overall, a variation in chemistry that indicated that the spinodal decomposition had occurred in the early stages of aging (Fig. 4d).

In samples aged for longer time, low magnification HAADF-STEM images showed a contrast resulting from spinodal decomposition. In sample SA2, which was subjected to 645 °C for 60 min, we could observe many bright patches, each about 10 nm in size, of an $\alpha_1$ phase that was rich in Fe and/or Co. These patches were homogeneously distributed throughout the surrounding dark matrix of an $\alpha_2$ phase that was rich in Cr (Fig. 5a). We also observed similar microstructure in further step-aged samples SA3-SA7 (Fig. 5b-f). As step aging progressed, especially in samples SA4, SA5, SA6, and SA7, the $\alpha_1$ phase became more distinct from the $\alpha_2$. These results may reflect an increase in the composition difference that occurred between the $\alpha_1$ and $\alpha_2$ phases with increased aging.

The results showed that, at medium stages of aging, four samples SA2-SA5 had microstructure that was broadly representative of all stages (Cf Figs. 4 and 5). We used atomic scale HAADF-STEM images of these samples to analyze atomic characteristics between the $\alpha_1$ and $\alpha_2$ phases formed during spinodal decomposition (Fig. 6). The *Z*-contrast intensity gradually increased overall from the $\alpha_2$ phase to the $\alpha_1$ phase, indicating no sharp interface between the two phases. We chose the maximum intensity ratio between the $\alpha_1$ and $\alpha_2$ in each of the four samples. This ratio gradually increased as step aging progressed, indicating that more diffusion occurred as aging time increased. We could clearly distinguish a dark region from a bright region as step aging progressed, especially in sample SA5 (Fig. 6 a3-d3). The schematic diagram of the distribution of Fe, Cr, and Co at different stages of heat treatment showed that the three elements were distributed in a disordered pattern throughout both $\alpha_1$ and $\alpha_2$ phases. Fe, Cr, and Co each fluctuated together when spinodal decomposition occurred. As step aging progressed, regions enriched in each of the three elements increased in size (Fig. 7).

Using Image Pro-Plus software, we measured the size and volume fraction of the $\alpha_1$ phase in samples SA2-SA7 (Fig. 8). The results indicated that the size of the $\alpha_1$ phase increased as step aging progressed. The volume fraction of the $\alpha_1$ phase, however, increased only from step 2 to step 4, but remained practically unchanged from step 4 to step 7.

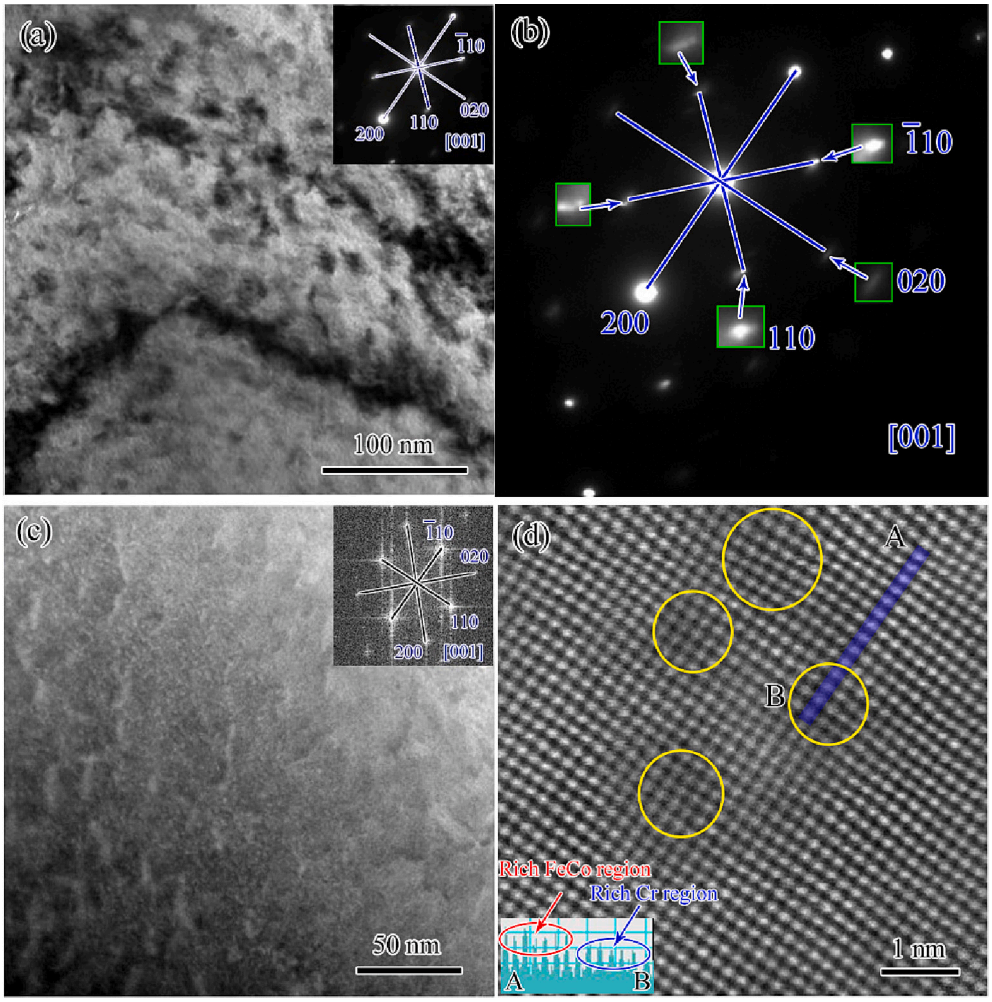

**Fig. 4.** TEM and HAADF-STEM images of sample SA1 (step 1: 645 °C for 10 min), as viewed along [001]. (a) Bright field TEM image with insert SADP image. (b) SADP image. The insets showed in green rectangles are from enlarged diffraction spots. The original locations of these spots are indicated by arrows. These enlarged spots are composed of two partially overlapped spots, indicating an occurrence of spinodal decomposition. (c) Low magnification HAADF-STEM image. (d) Atomic scale HAADF-STEM image. The insert shows the intensity profile of values taken from each atom along the blue line from a dark region (shown in the yellow circles) to a bright region, with the greatest intensity ratio between bright and dark at about 1.5 ± 0.1. (For interpretation of the references to colour in this figure legend, the reader is referred to the web version of this article.)

### 3.4. Analysis of evolution of composition

Because spinodal decomposition has no barrier to nucleate, it is a rapid diffusion process. Using EDS-SI maps, we analyzed the composition evolution between the $\alpha_1$ and $\alpha_2$ phases in samples taken at earlier and later stages of spinodal decomposition. We used sample SA1 (step 1, aged at 645 °C for 10 min) to analyze the fluctuations of elements at the early stage. The EDS results showed that Fe, Cr, and Co each fluctuated together within areas about 2 nm wide, indicating that the wavelength was very small in the early stage of spinodal decomposition (Fig. 9a2). That explained why we did not observe a clear $\alpha_1$ phase in the HAADF-STEM image of the same sample (Fig. 4c). In the EDS maps of sample SA2 (Step 2, aged at 645 °C for 60 min), we could clearly observe the contrast between rich and poor elements in adjacent regions, each about 10 nm wide. This indicated that the fluctuations of elements here had a larger wavelength than in sample SA1, making it possible to clearly distinguish the $\alpha_1$ phase in the HAADF-STEM image in sample SA2. In sample SA3-SA7, we could also observe this contrast (Fig. 9).

Close examination of the EDS results of the $\alpha_1$ and $\alpha_2$ showed that, from sample SA1 to sample SA6 of the aging process, the degree of enrichment of the dominant elements of both phases increased steadily. From sample SA6 to sample SA7, however, certain elements either decreased or increased. For example, the concentration of Co in the $\alpha_1$ phase decreased from sample SA6 to sample SA7, although the concentration of Fe continued its steady increase. Similarly, the concentration of Cr, which had steadily decreased from sample SA1 to sample SA6, actually increased from sample SA6 to sample SA7. By contrast, in the $\alpha_2$ phase, the concentration of Fe gradually decreased from sample SA1 to sample SA7, but the concentration of Cr decreased from sample SA6 to sample SA7. Similarly, the concentration of Co, which had steadily decreased from step 1 to step 6, actually increased from sample SA6 to sample SA7 (Fig. 10).

In previous study, we measured the chemistry of FeCrCo samples, using line EDS in STEM and confirmed that we could use both amplitude (A) and wavelength (λ) in cosine function to describe the late stage of spinodal decomposition [40]. Other researchers have studied the relationship between λ and aging time in Cu30Ni2.5Cr and Cu45Ni10Cr alloys annealed from 300 °C to 800 °C. Their results showed that λ remained constant in the initial stage of spinodal decomposition, but increased later as aging time increased [54]. To analyze the evolution of wavelength in different step-aged samples, using HAADF-STEM images, we measured the sizes of the $\alpha_1$ and $\alpha_2$ phases to calculate the wavelength (Fig. 11). Since the $\alpha_1$ phase of sample SA1 (step 1: 645 °C 10 min) in the HAADF-STEM images was too small to be seen, we analyzed the wavelength evolution in samples SA2-SA7. The results showed that the wavelength increased as step aging progressed. The wavelength increased by 86.7% from sample SA2 to sample SA3, 7.1% from sample SA3 to sample SA4, 6.7% from sample SA4 to sample SA5, 6.3% from sample SA5 to sample SA6, and 17.6% from sample SA6 to sample SA7. This indicated that the wavelength increased faster in the early stages of high temperature step aging.

We also analyzed the amplitudes of element fluctuation of Fe, Cr, and Co in samples SA1-SA7 (Fig. 12). The results showed that, in the $\alpha_1$ phase, the amplitude of Fe increased almost linearly from sample SA1 to

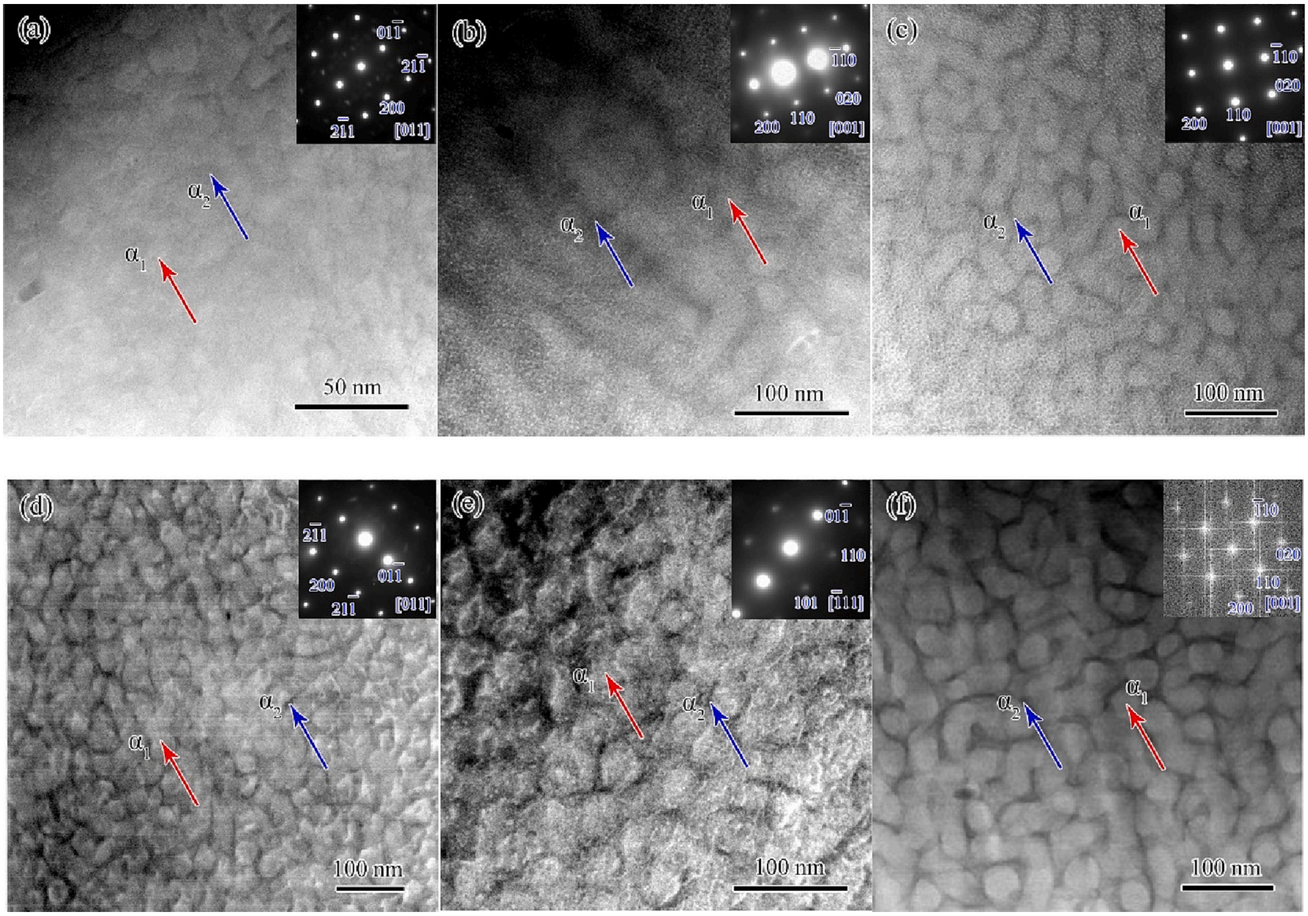

**Fig. 5.** Low magnification HAADF-STEM images of samples SA2-SA7. (a) Sample SA2 (step 2: 645 °C 1 h). (b) Sample SA3 (step 3: step 2 + 620 °C 1 h). (c) Sample SA4 (step 4: step 3 + 600 °C 2 h). (d) Sample SA5 (step 5: step 4 + 580 °C 3 h). (e) Sample SA6 (step 6: step 5 + 560 °C 4 h). (f) Sample SA7 (step 7: step 6 + 540 °C 5 h + 520 °C 6 h). Bright patches of the $\alpha_1$ phase regions are indicated by red arrows. The $\alpha_1$ phase regions are distributed throughout the surrounding dark matrix of the $\alpha_2$ phase indicated by blue arrows. (For interpretation of the references to colour in this figure legend, the reader is referred to the web version of this article.)

sample SA7. The amplitude of Cr and Co also increased almost linearly, but only from sample SA1 to sample SA6, decreasing thereafter from sample SA6 to sample SA7 (Fig. 12a). In the $\alpha_2$ phase, the amplitude of Fe increased, but not necessarily linearly, from sample SA1 to sample SA7. The amplitude of Cr also increased not necessarily linearly from sample SA1 to sample SA6, decreasing thereafter from sample SA6 to sample SA7, but the amplitude increase ratios of Fe and Cr from sample SA3 to sample SA4 were disproportionately large. The amplitude of Co increased almost linearly from sample SA1 to sample SA6, then decreased from sample SA6 to sample SA7 (Fig. 12b). For Fe, the average amplitude in both phases increased with step aging. For Cr and Co, however, the average amplitude increased with step aging only up to sample SA6. From sample SA6 to sample SA7, the average amplitude decreased even though step aging had progressed (Fig. 12c).

## 4. Discussion

### 4.1. Effect of step aging on hardness

Previous researchers have found that the increment in hardness resulting from spinodal decomposition is closely related to the periodic diffusion of elements in spinodal alloys [55–57]. Our EDS results showed fluctuations of all three elements in all step-aged samples SA1-SA7 (Fig. 9). Because of these fluctuations, the Vickers hardness of solution-treated samples after step aging gradually increased from sample SA1 to sample SA6, then decreased marginally from sample SA6 to sample SA7 (Fig. 2a). These changes in hardness reflected changes in the amplitude and wavelength of spinodal decomposition. Chan et al. [58] and Schwartz et al. [59] found that hardness increased as amplitude and wavelength of the spinodal decomposition. Other researchers, however, found that hardness increased with an amplitude increase but decreased when the wavelength increased [60,61]. The hardness and microstructure data, reported in a previous study, support the latter conclusion [40].

In samples SA1-SA7, both the spinodal decomposition wavelength and amplitude of Fe, Cr, and Co gradually increased from sample SA1 to sample SA6 (Figs. 11 and 12). Consequently, hardness increased from sample SA1 to sample SA6 (Fig. 2a). The fact that the hardness decreased marginally from sample SA6 to sample SA7, however, may reflect the simultaneous decrease in amplitude and increase in wavelength of both Cr and Co that occurred at that point. The test data showed that hardness increased most (17.4%) from sample SA3 to sample SA4. Meanwhile, the amplitude ratio of Fe and Cr increased most from sample SA3 to sample SA4. This confirms that the spinodal decomposition amplitude plays a leading role in hardness.

Kato calculated the incremental critical resolved shear stress (ΔCRSS) for Fe-Cr binary alloys using the following formula [61]:

$$\Delta\mathrm{CRSS} = A\eta Y/2 + 0.65\Delta \mathrm{G}b/\lambda \tag{1}$$

The first term, $A\eta Y/2$, represents the misfit-hardening effect, where $A$ is the amplitude, $Y$ the elastic constant, and $\eta$ a coefficient describing the coherency strain by the lattice misfit, the value for $\eta$ is derived as follows [62]:

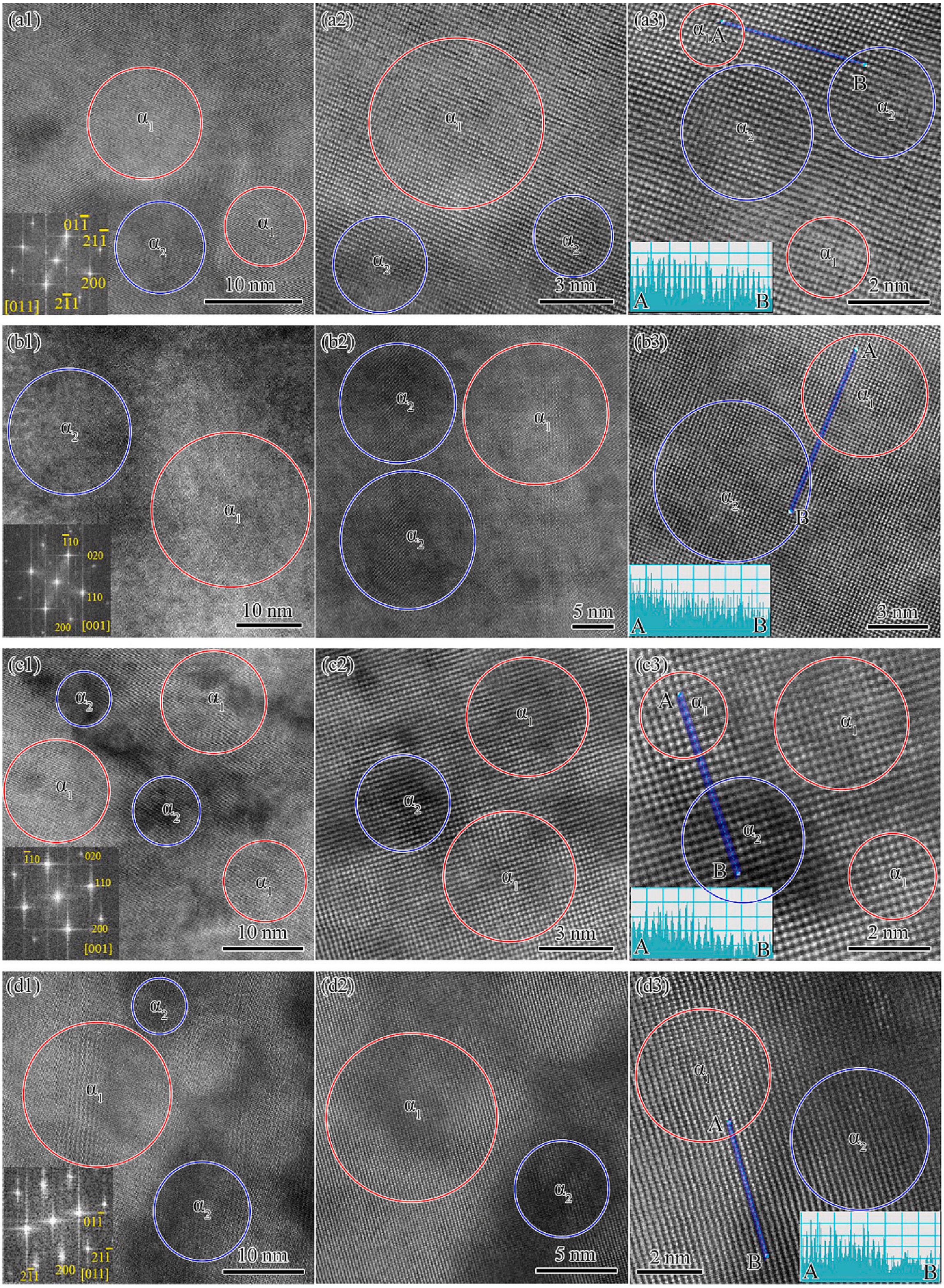

**Fig. 6.** Analysis of atomic resolution HAADF-STEM images of samples SA2-SA5. Low (a1), medium (a2) and high (a3) magnification images of the $\alpha_1$ and $\alpha_2$ phases in sample SA2, as viewed along [011]. Low (b1), medium (b2) and high (b3) magnification images of the $\alpha_1$ and $\alpha_2$ phases in sample SA3, as viewed along [001]. Low (c1), medium (c2) and high (c3) magnification images of the $\alpha_1$ and $\alpha_2$ phases in sample SA4, as viewed along [001]. Low (d1), medium (d2) and high (d3) magnification images of the $\alpha_1$ and $\alpha_2$ phases in sample SA5, as viewed along [011]. The insets show the intensity profile of values taken from each atom along the line AB from a dark region to a bright region (a3-d3). The greatest intensity ratio between bright and dark of samples SA2, SA3, SA4 and SA5 at about 1.21 ± 0.1, 1.43 ± 0.2, 1.51 ± 0.1 and 1.56 ± 0.1, respectively. Red circles correspond to the area of the $\alpha_1$ phase, blue circles to the area of the $\alpha_2$ phase. (For interpretation of the references to colour in this figure legend, the reader is referred to the web version of this article.)

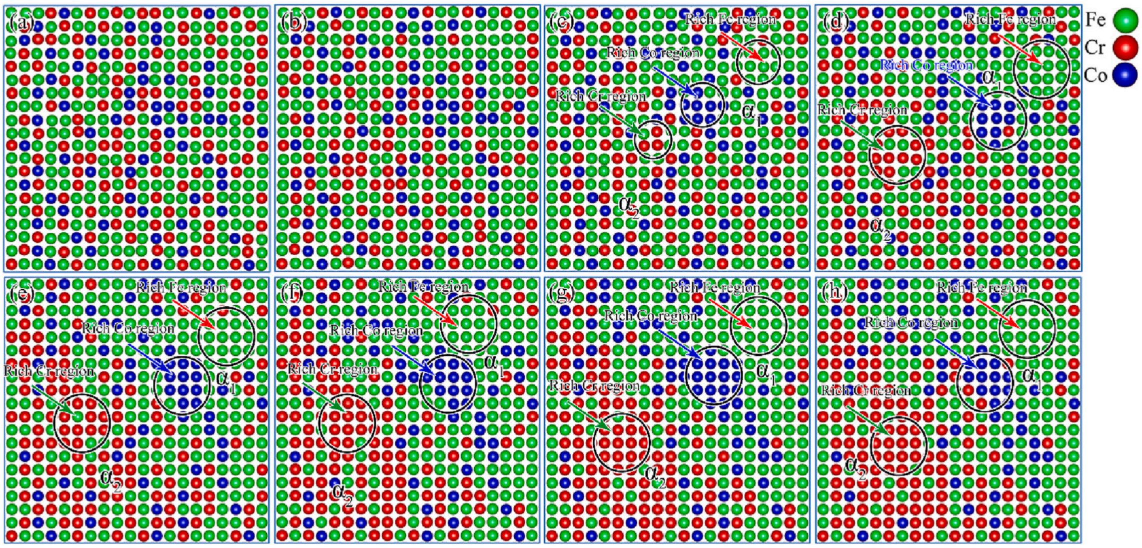

**Fig. 7.** Schematic diagram of evolution of atomic structure between the $\alpha_1$ and $\alpha_2$ phases during the process of step aging. (a) No step aging. The Fe, Cr, and Co are uniformly distributed throughout the α matrix. (b) Step 1. The three atoms do not clearly rich together. (c)-(h) correspond to step 2, step 3, step 4, step 5, step 6, and step 7, respectively. The Fe and Co are rich in the $\alpha_1$ phase. The Cr is rich in the $\alpha_2$ phase. The rich regions of the three atoms are increase from step 1 to step 6, and remain unchanged from step 6 to step 7. The three elements are disorderly distributed between the $\alpha_1$ and $\alpha_2$ phases.

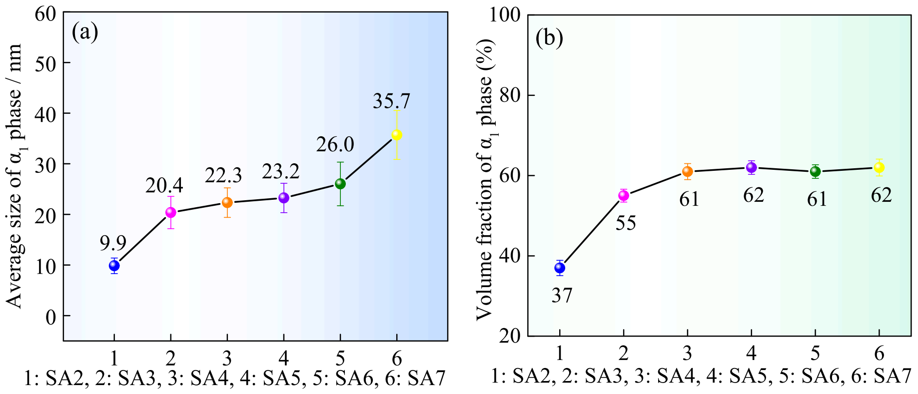

**Fig. 8.** Size and volume of the $\alpha_1$ phase of samples SA2-SA7. (a) The size of the $\alpha_1$ phase. (b) The volume fraction of the $\alpha_1$ phase.

$$\eta = \frac{\Delta a}{2Aa_0} \tag{2}$$

where $\Delta a/a_0$ is the misfit between the lattice constants for the $\alpha_1$ and $\alpha_2$ phases. The second term, $0.65\Delta Gb/\lambda$, represents the modulus-hardening effect induced by composition variations, where $\lambda$ is the wavelength, b the magnitude of the Burgers vector, and $\Delta G$ the amplitude of the shear modulus change.

In previous study, we calculated the ΔCRSS for Fe-Cr-Co ternary alloys using a formula derived from Eq. (1) as follows [40]:

$$\Delta CRSS_{\mathrm{Fe-Cr-Co}} = ((\mathrm{Fe-Cr})\ \mathrm{vol\%})\ \Delta CRSS_{\mathrm{Fe-Cr}} + ((\mathrm{Fe-Co})\ \mathrm{vol\%})\ \Delta CRSS_{\mathrm{Fe-Co}} \tag{3}$$

$$\Delta CRSS_{\mathrm{Fe-Cr}} = A_{\mathrm{Cr}}\ \eta Y/2 + 0.65\Delta \mathrm{G}_{\mathrm{Fe-Cr}}\mathrm{b}/\lambda \tag{4}$$

$$\Delta CRSS_{\mathrm{Fe-Co}} = A_{\mathrm{Co}}\ \eta Y/2 + 0.65\Delta \mathrm{G}_{\mathrm{Fe-Co}}\mathrm{b}/\lambda \tag{5}$$

The calculated results were similar to our experimental results.

Eq. (2) indicates that hardness increases with an increase in the degree of the lattice misfit. Using atomic resolution HAADF-STEM images to study the evolution of lattice misfit during step aging, we measured the lattice spacing in both $\alpha_1$ and $\alpha_2$ phases in two directions for samples SA1, SA2, SA3, SA4, and SA5 (Fig. 13 and Table 2). Using these values, we calculated the lattice constants in the $\alpha_1$ and $\alpha_2$ phases for samples SA1-SA5 (Table 2). For each sample, the calculated lattice constants varied, depending on direction and phase. For example, the lattice constant in one direction in the $\alpha_1$ phase might be smaller than in the other direction in the $\alpha_2$ phase. In the same direction, however, the lattice constant in the $\alpha_1$ phase might be larger than in the $\alpha_2$ phase. This difference in calculated lattice constant may be the result of imaging distortion or lattice distortion. We therefore calculated the average lattice constant in two directions for the $\alpha_1$ and $\alpha_2$ phases, then calculated the lattice misfit between the two phases for samples SA1-SA5 (Fig. 13f). The results showed that the value of lattice misfit gradually increased in samples SA1-SA5 indicating that the degree of lattice misfit increased as step aging progressed. This may explain why hardness increased with the duration of step aging during the first five steps.

### *4.2. Effect of step aging on magnetic properties*

Room-temperature magnetic properties measurement data for each step-aged samples SA1-SA7 showed that, from sample SA1 to sample SA6, the values of remanence and coercivity gradually increased as step aging progressed (Fig. 14a). The changes in magnetic properties may be

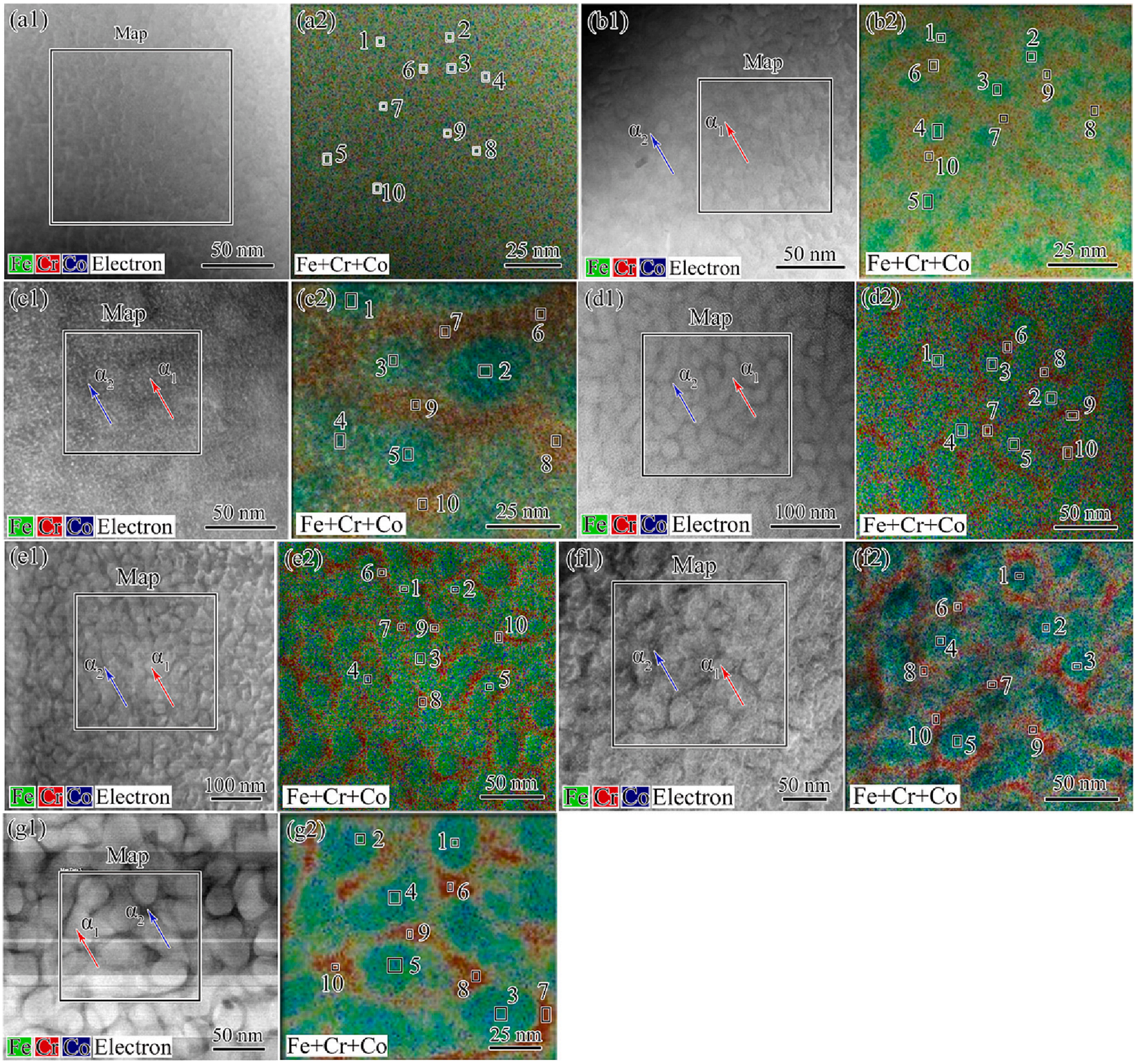

**Fig. 9.** HAADF-STEM images and EDS maps scan profiles in samples SA1-SA7. (a1)-(g1) HAADF-STEM images of the $\alpha_1$ and $\alpha_2$ phases in samples SA1-SA7. EDS probe is scanned in the map indicated in the figures. (a2)-(g2) Superimposed EDS maps of Fe, Cr, and Co in samples SA1-SA7.

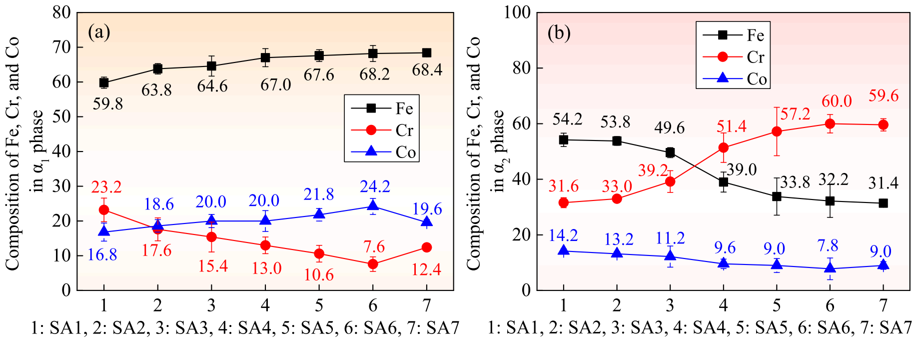

**Fig. 10.** Compositions evolution of Fe, Cr, and Co in the $\alpha_1$ and $\alpha_2$ phases in samples SA1-SA7. (a) In the $\alpha_1$ phase; (b) In the $\alpha_2$ phase. Using superimposed EDS map of each sample (Fig. 9 a2–g2), we measured 1, 2, 3, 4, 5 EDS maps to analyze the compositions evolution of the three elements in the $\alpha_1$ phase, and 6, 7, 8, 9, 10 EDS maps to analyze compositions evolution of the three elements in the $\alpha_2$ phase. The composition of each EDS map is shown in Table 1.

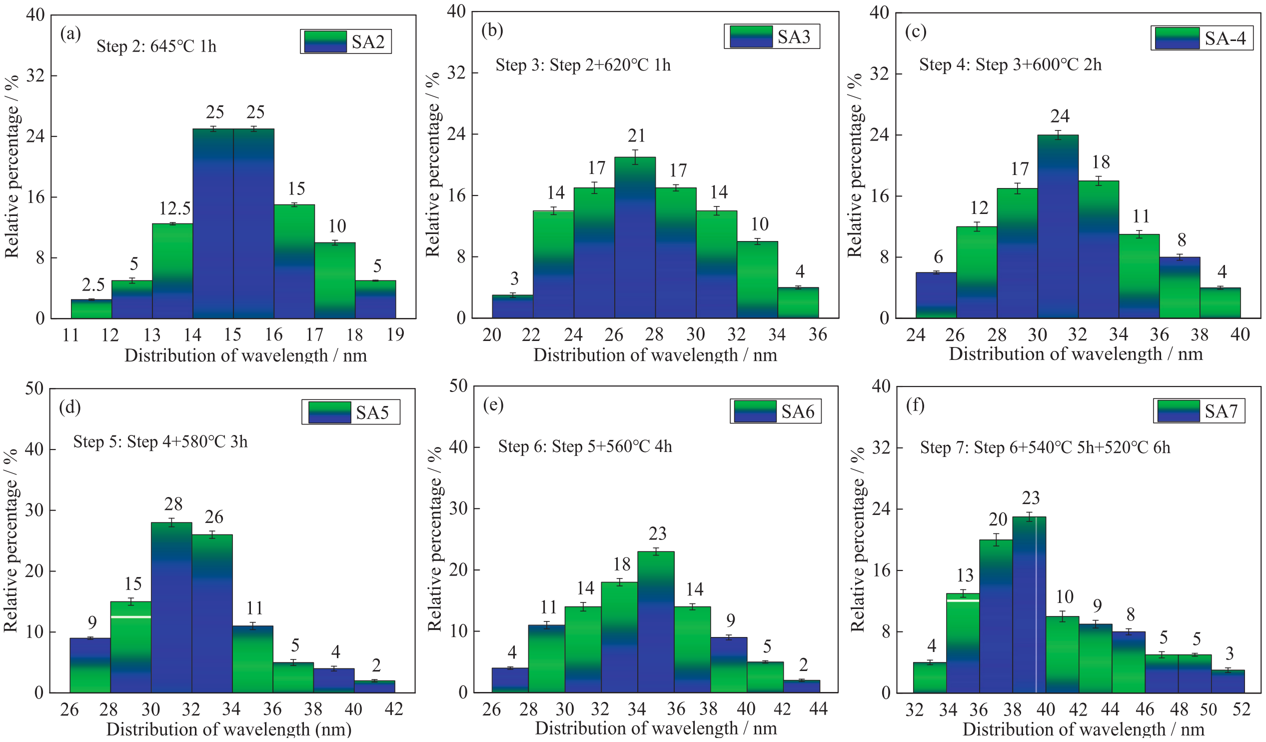

**Fig. 11.** Wavelength distributions of samples SA2-SA7. (a) Sample SA2. Average wavelength is 15 ± 1.5 nm. (b) Sample SA3. Average wavelength is 28 ± 3.2 nm. (c) Sample SA4. Average wavelength is 30 ± 2.9 nm. (d) Sample SA5. Average wavelength is 32 ± 2.9 nm. (e) Sample SA6. Average wavelength is 34 ± 4.3 nm. (f) Sample SA7. Average wavelength is 40 ± 4.6 nm.

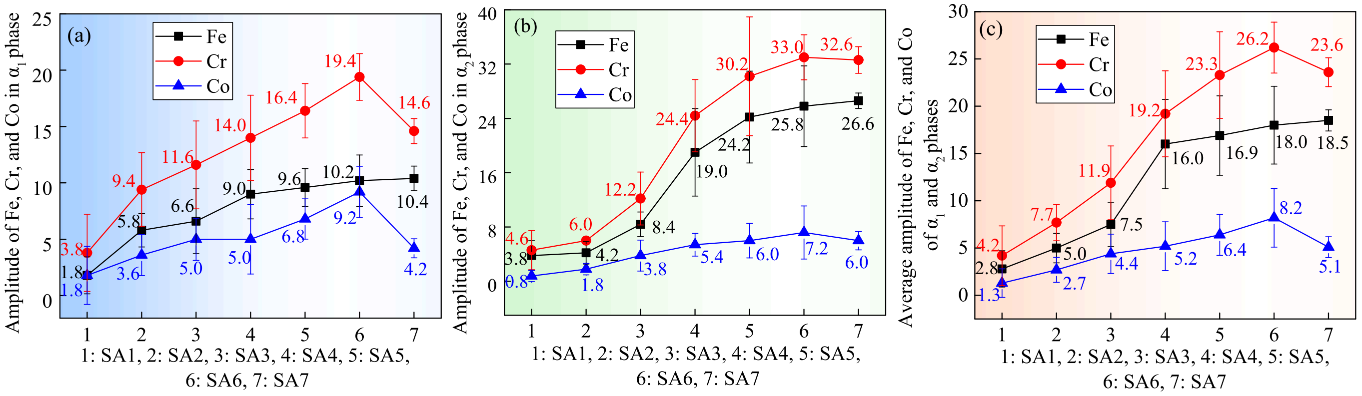

**Fig. 12.** Amplitudes of Fe, Cr, and Co of samples SA1-SA7. (a) Amplitudes of Fe, Cr, and Co in the $\alpha_1$ phases. (b) Amplitudes of Fe, Cr, and Co in the $\alpha_2$ phases. (c) Average amplitudes of the $\alpha_1$ and $\alpha_2$ phases. Before step aging, the original concentrations of Fe, Cr, and Co were 58%wt, 27%wt, and 15%wt, respectively. Using overlay EDS map of each sample (Fig. 9 a2–g2), we measured 1, 2, 3, 4, 5 EDS maps to analyze the amplitudes of Fe, Cr, and Co in $\alpha_1$ for each sample, and 6, 7, 8, 9, 10 EDS maps to analyze the amplitudes of Fe, Cr, and Co in $\alpha_2$ for each sample. The composition of each EDS map was shown in Table 1. We also analyzed the average amplitude of the two phases for each sample.

related to the volumes, sizes, and compositions of the $\alpha_1$ and $\alpha_2$ phases and to the composition difference between the two phases.

The $\alpha_1$ phase is ferromagnetic, indicating that its magnetic properties are proportional to its volume. The HAADF-STEM results showed that the volume of the $\alpha_1$ phase kept increasing from sample SA1 (step 1) to sample SA4 (step 4), leading to a significant increase in remanence and coercivity during those steps (Figs. 14a and 8b). This increase showed that the volume of the $\alpha_1$ phase played an important role in developing magnetic properties at the early stages of spinodal decomposition. We found that the volume of the $\alpha_1$ phase remained unchanged from sample SA4 to sample SA7, even though remanence and coercivity still continued to increase from sample SA4 to sample SA6. We concluded that, although volume fraction was an important parameter during the first four steps, other microstructure parameters became more important in the later stages of step aging.

It was reported that a refined microstructure could pin the movement of domain walls, resulting in an increase in magnetic properties of $MRE_2(Fe, Co)_{14}B$ [63], NdFeB [64] and SmCo [65] alloys. Consequently, we assumed that refined $\alpha_1$ particles could increase the magnetic properties of FeCrCo alloys. The results showed that the size of $\alpha_1$ particles kept increasing from sample SA1 to sample SA7 (Fig. 8a). Both coercivity and remanence, however, kept increasing from sample SA1 to sample SA6 (Fig. 14a). These results indicated that the magnetic properties for each step-aged sample were connected not only to the size and volume of the $\alpha_1$ phase but also to the compositions of both $\alpha_1$ and $\alpha_2$ phases.

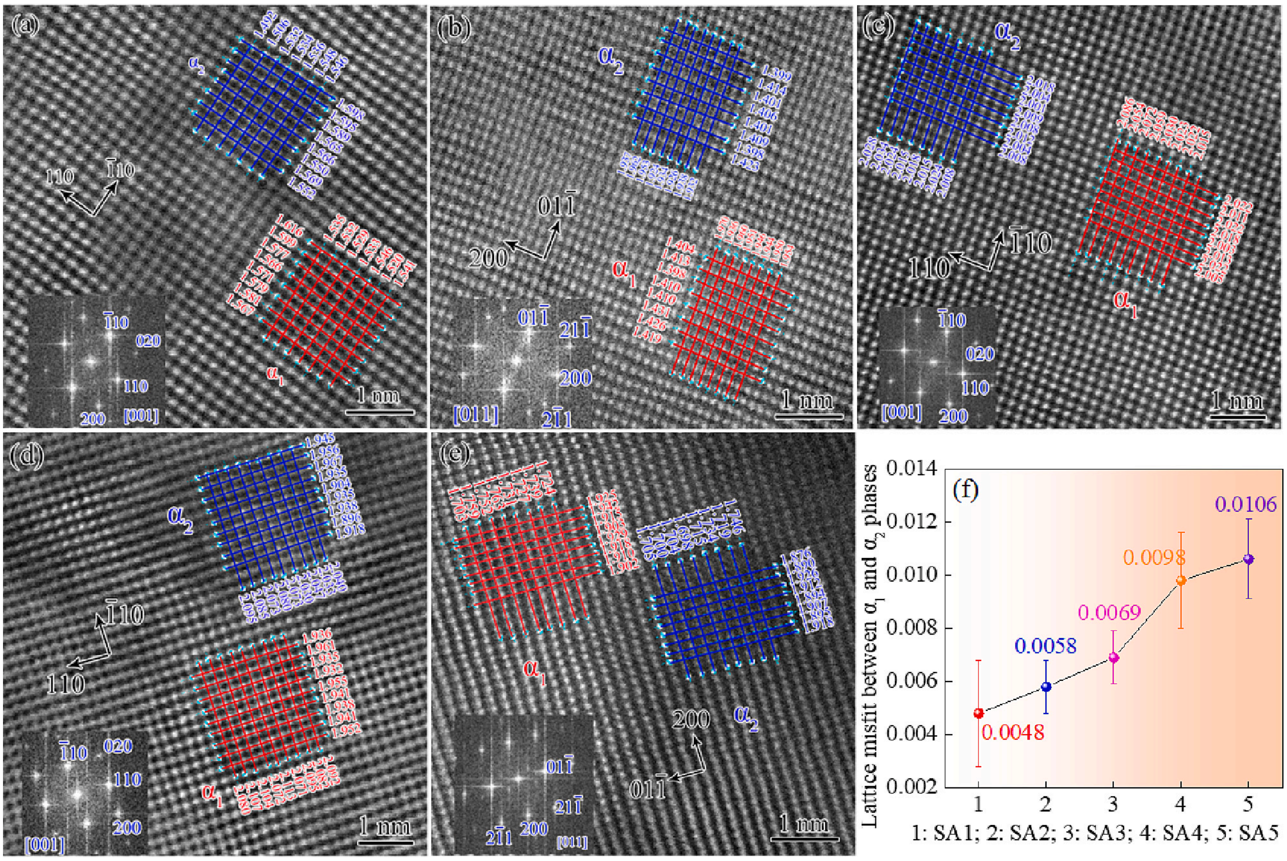

**Fig. 13.** Analysis of lattice spacing and lattice misfit between the $\alpha_1$ and $\alpha_2$ phases in samples SA1-SA5. All the atomic HAADF-STEM images contain both $\alpha_1$ and $\alpha_2$ phases. Fig. a. Lattice spacing of the $\alpha_1$ (bright regions) and the $\alpha_2$ (dark regions) phases are measured in (110) and (−110) in sample SA1. Fig. b. Lattice spacing of the $\alpha_1$ (bright regions) and the $\alpha_2$ (dark regions) phases are measured in (200) and (01−1) in sample SA2. Fig. c. Lattice spacing of the $\alpha_1$ (bright regions) and the $\alpha_2$ (dark regions) phases are measured in (110) and (−110) in sample SA3. Fig. d. Lattice spacing of the $\alpha_1$ (bright regions) and the $\alpha_2$ (dark regions) phases are measured in (110) and (−110) in sample SA4. Fig. e. Lattice spacing of the $\alpha_1$ (bright regions) and the $\alpha_2$ (dark regions) phases are measured in (200) and (01–1) in sample SA5. For all the samples, the lattice spacing in the $\alpha_1$ phase are measured along red lines, and in the $\alpha_2$ phase is measured along blue lines. The average lattice spacing values are shown in Table 2. Fig. f. The value of lattice misfit in samples SA1-SA5. (For interpretation of the references to colour in this figure legend, the reader is referred to the web version of this article.)

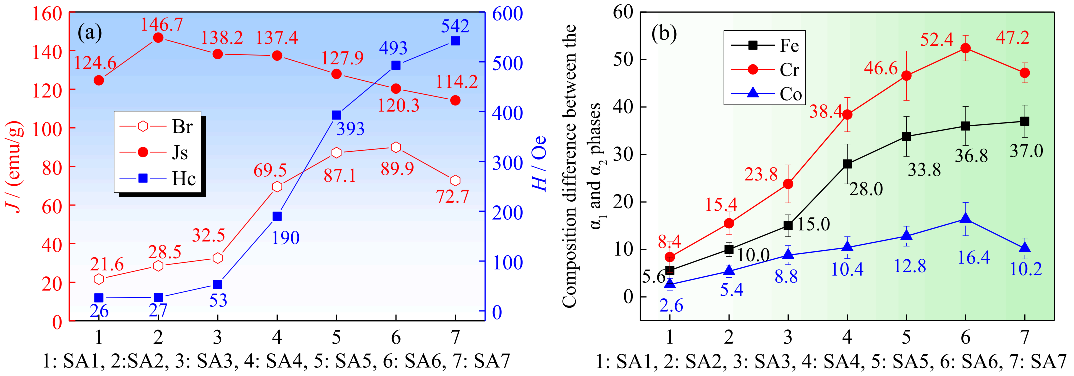

**Fig. 14.** Magnetic properties and composition difference between the $\alpha_1$ and $\alpha_2$ phases of samples SA1-SA7. (a) Remanence (*Br*), intrinsic coercivity (*Hc*), and saturation polarization ($J_S$) of samples SA1-SA7. The values of *Br*, *Hc*, and $J_S$ are extracted from curves in Fig. 2b. (b) Composition difference between the $\alpha_1$ and $\alpha_2$ phases of samples SA1-SA7. The values of composition difference of three elements are extracted from the data in Fig. 10.

For $Nd_2Fe_{14}B$, some researchers found that substitution of Co for Fe could increase Tc, even though the moment of Co (1.6 $\mu_B$) is lower than that of Fe (2.2 $\mu_B$). They also found that the saturation magnetization increased with Co increased up to 30%, and then decreased with Co further increase [66]. For $(Nd_{1-x}Ce_x)_2Fe_{1-y}Co_yB$, other researchers revealed that the permanent magnetic properties were significantly enhanced but only for a critical concentration of Co [67]. For FeCrCo alloys, at low cobalt contents (5 wt%-9 wt%), it was found that both remanence and coercivity increased with Co increase [3,31]. At higher cobalt contents (15 wt%-20 wt%), other researchers have confirmed this conclusion [30,68]. The magnetic properties are dominated by the ferromagnetic $\alpha_1$ phase (rich Fe-Co) for FeCrCo alloys [13]. We infer that the concentration of Co in the $\alpha_1$ phase plays an important role for the magnetic properties of FeCrCo alloys.

**Table 1**
Composition of each map of samples SA1-SA7. Average compositions of the $\alpha_1$ in samples SA1-SA7 are 59.8Fe23.2Cr16.8Co, 63.8Fe17.6Cr18.6Co, 64.6Fe15.4Cr20Co, 67.0Fe13.0Cr20.0Co, 67.6Fe10.6Cr21.8Co, 68.2Fe7.6Cr24.2Co, and 68.4Fe12.4Cr19.2Co, respectively. Average compositions of the $\alpha_2$ in samples SA1-SA7 are 54.2Fe31.6Cr14.2Co, 53.8Fe33.0Cr13.2Co, 49.6Fe39.2Cr11.2Co, 39.0Fe51.4Cr9.6Co, 33.8Fe57.2Cr9.0Co, 32.2Fe60.0Cr7.8Co, and 31.4Fe59.6Cr9.0Co, respectively.

| Sample | Maps in the $\alpha_1$ phase (wt%) | | | | |
|---|---|---|---|---|---|
| | Map 1 | Map 2 | Map 3 | Map 4 | Map 5 |
| SA1 | 58Fe22Cr20Co | 61Fe20Cr18Co | 59Fe29Cr12Co | 61Fe23Cr16Co | 60Fe22Cr18Co |
| SA2 | 64Fe17Cr19Co | 63Fe19Cr18Co | 64Fe17Cr19Co | 62Fe22Cr16Co | 66Fe13Cr21Co |
| SA3 | 65Fe17Cr18Co | 65Fe13Cr22Co | 68Fe11Cr21Co | 65Fe14Cr21Co | 60Fe22Cr18Co |
| SA4 | 66Fe11Cr23Co | 71Fe13Cr16Co | 64Fe17Cr19Co | 68Fe13Cr19Co | 66Fe11Cr23Co |
| SA5 | 68Fe9Cr23Co | 66Fe14Cr20Co | 66Fe10Cr24Co | 70Fe8Cr22Co | 68Fe12Cr20Co |
| SA6 | 71Fe6Cr22Co | 67Fe11Cr22Co | 69Fe6Cr26Co | 65Fe8Cr27Co | 69Fe7Cr24Co |
| SA7 | 70Fe12Cr18Co | 69Fe11Cr20Co | 68Fe13Cr19Co | 68Fe12Cr20Co | 67Fe14Cr19Co |
| Sample | Maps in the $\alpha_2$ phase (wt%) | | | | |
| | Map 6 | Map 7 | Map 8 | Map 9 | Map 10 |
| SA1 | 53Fe32Cr15Co | 53Fe33Cr14Co | 55Fe30Cr15Co | 52Fe34Cr14Co | 58Fe29Cr13Co |
| SA2 | 53Fe34Cr13Co | 55Fe33Cr12Co | 54Fe33Cr13Co | 53Fe33Cr14Co | 54Fe32Cr14Co |
| SA3 | 48Fe43Cr9Co | 51Fe38Cr11Co | 48Fe41Cr11Co | 52Fe33Cr15Co | 49Fe41Cr10Co |
| SA4 | 37Fe53Cr10Co | 47Fe45Cr8Co | 31Fe59Cr10Co | 44Fe48Cr8Co | 36Fe52Cr12Co |
| SA5 | 31Fe62Cr7Co | 42Fe45Cr13Co | 25Fe68Cr7Co | 39Fe53Cr8Co | 32Fe58Cr10Co |
| SA6 | 32Fe59Cr9Co | 29Fe61Cr10Co | 29Fe63Cr8Co | 41Fe56Cr3Co | 30Fe61Cr9Co |
| SA7 | 33Fe57Cr10Co | 28Fe62Cr10Co | 32Fe58Cr10Co | 33Fe60Cr7Co | 31Fe61Cr8Co |

**Table 2**
Average lattice spacing and lattice constant of samples SA1, SA2, SA3, SA4, and SA5, respectively.

| Phase | SA1 | SA2 | SA3 | SA4 | SA5 |
|---|---|---|---|---|---|
| Lattice spacing (nm) | | | | | |
| In $\alpha_1$ | (110): 0.1917 ± 0.0009 | (01–1): 0.1414 ± 0.0009 | (110): 0.1859 ± 0.001 | (110): 0.1943 ± 0.001 | (01–1): 0.1448 ± 0.0009 |
| | (−110): 0.1978 ± 0.0009 | (200): 0.1951 ± 0.0009 | (−110): 0.2015 ± 0.002 | (−110): 0.2091 ± 0.002 | (200): 0.1918 ± 0.0007 |
| In $\alpha_2$ | (110): 0.1909 ± 0.001 | (0–1): 0.1406 ± 0.0008 | (110): 0.1837 ± 0.001 | (110): 0.1933 ± 0.001 | (01–1): 0.1429 ± 0.0008 |
| | (−110): 0.1966 ± 0.002 | (200): 0.1939 ± 0.0009 | (−110): 0.2008 ± 0.002 | (−110): 0.2062 ± 0.002 | (200): 0.1902 ± 0.0009 |
| Lattice constant (nm) | | | | | |
| In $\alpha_1$ | (110):0.2711 ± 0.0015 | (01–1): 0.2828 ± 0.0022 | (110): 0.2625 ± 0.0033 | (110): 0.2957 ± 0.0021 | (01–1): 0.2895 ± 0.0033 |
| | (−110):0.2797 ± 0.0030 | (200): 0.2760 ± 0.0014 | (−110): 0.2849 ± 0.0011 | (−110): 0.2748 ± 0.0014 | (200): 0.2712 ± 0.0028 |
| In $\alpha_2$ | (110):0.2701 ± 0.0037 | (01–1):0.2813 ± 0.0017 | (110): 0.2598 ± 0.0011 | (110): 0.2916 ± 0.0034 | (01–1): 0.2858 ± 0.0019 |
| | (−110):0.2781 ± 0.0033 | (200): 0.2742 ± 0.0018 | (−110): 0.2840 ± 0.0007 | (−110): 0.2733 ± 0.0032 | (200): 0.2690 ± 0.002 |

Using STEM-EDS maps, we analyzed the composition of the $\alpha_1$ phase in each step-aged sample (Fig. 10 and Table 1). The results showed that the concentration of Cr decreased as step aging progressed but increased from sample SA6 to sample SA7. The concentration of Fe increased as step aging progressed, however, the concentration of Co kept increasing from sample SA1 to sample SA6, but decreased from sample SA6 to sample SA7 (Fig. 10). The results showed that the magnetic properties were improved with the concentrations of Fe and Co increasing. The remanence decreased from sample SA6 to sample SA7 may be related to the decrease in the concentration of ferromagnetic Co and the increase of non-ferromagnetic Cr in the $\alpha_1$ phase. Previous researchers [69] studied the effect of Co on magnetic properties of $Nd_2(FeCo)_{14}B/\alpha$-Fe and found that both remanence and maximum energy product have remarkably enhanced with the Co increase, but the coercivity decreased. The EDS results showed that the intensity of Co in the $\alpha_1$ phase decreased from sample SA6 to sample SA7, contributing to a decrease in the remanence, but an increase in coercivity.

Based on the model for theoretical hysteresis curves of interacting among ellipsoids analyzed by Stoner and Wohlfarth [70], Drapal derived a formula to calculate the $H_c$ between strongly magnetic $\alpha_1$ particles and weakly magnetic $\alpha_2$ matrix for FeCrCo alloys as follows [71]:

$$H_c = p(1-p)(N_b - N_a)\frac{(J_{s\alpha1} - J_{s\alpha2})^2}{\mu_0 J_s} \tag{6}$$

where $p$ is the volume fraction of the $\alpha_1$ phase, $J_{s\alpha1}$ and $J_{s\alpha2}$ are the saturation magnetic polarizations of the $\alpha_1$ and $\alpha_2$ phases, respectively, $N_a$ and $N_b$ are the demagnetizing factors of the $\alpha_1$ phase along the a and b axes, $J_s$ is the saturation polarization of the alloy, and $\mu_0$ is the permeability of a vacuum.

According to Eq. (6), the coercivity depends on the value of $p$, on the shape anisotropy of the $\alpha_1$ phase, $N_b - N_a$, on the difference between the saturation polarizations of the $\alpha_1$ and $\alpha_2$ phases, $J_{s\alpha1} - J_{s\alpha2}$, and on the saturation polarization of the alloy, $J_s$. The HAADF-STEM results showed that the shape of the $\alpha_1$ phase in all step-aged samples SA1-SA7 was spherical, indicating that the value for $N_b$-$N_a$ was identical (Fig. 5). In samples SA4-SA7, those from the later stages of step aging, the volume of the $\alpha_1$ phase remained unchanged, showing that the value for $H_c$ was determined by the value of $(J_{s\alpha1} - J_{s\alpha2})^2/J_s$. Since Fe and Co are ferromagnetic elements and Cr is a non-ferromagnetic element, the value of $J_s$ is larger for $\alpha_1$ than for $\alpha_2$. The STEM-EDS results showed that the differences in the levels of Fe, of Cr, and of Co between the $\alpha_1$ and $\alpha_2$ phases increased steadily from sample SA1 to sample SA6 (Fig. 14b). This increase reflected an increase in the value of $(J_{s\alpha1} - J_{s\alpha2})$, which may be the main reason for the increase in coercivity from sample SA1 to sample SA6. Eq. (6) also shows that the value for $H_c$ increases as $J_s$ decreases. The results of the hysteresis loops indicated that the value for $J_s$ decreased from sample SA6 to sample SA7 (Figs. 2b and 14a). This decrease may explain why the coercivity kept increasing from sample SA6 to sample SA7 despite a decrease in the composition difference between the $\alpha_1$ and $\alpha_2$ phases in these two samples (Fig. 14b).

Other researchers have found that magnetic properties are closely related to exchange coupling interactions between soft and hard phases and that the magnitude of exchange coupling interactions is related to the difference in saturation magnetization between the two phases [72–74]. For FeCrCo alloys, the Fe-Co-rich $\alpha_1$ phase is the hard phase, and the Cr- rich $\alpha_2$ phase is the soft phase. The composition difference between these two phases increased from sample SA1 to sample SA6 (Fig. 14b). This indicated an increase in the saturation magnetization difference, thus suggesting that the exchange coupling interaction strengthened as step aging progressed. This strengthening contributed to increases in both remanence and coercivity from sample SA1 to sample SA6, but the decrease in composition difference from sample SA6 to sample SA7 may have contributed to a corresponding decrease in remanence.

In further study, we found increases in coercivity of 3.8% from sample SA1 to sample SA2, 96% from sample SA2 to sample SA3, 258.5% from sample SA3 to sample SA4, 106.8% from sample SA4 to sample SA5, and 25.4% from sample SA5 to sample SA6, 9.9% from sample SA6 to sample SA7. The corresponding increases in remanence were 31.9%, 14.0%, 114.5%, 25%, and 3.2%, followed by a decrease from sample SA6 to sample SA7. Increases in both coercivity and remanence from sample SA3 to sample SA4 were much larger than any of other intervals, likely because the relative amplitude of composition fluctuations for both Fe and Cr was greater there (see Figs. 12 and 14).

## 5. Conclusions

The study of the evolution of microstructure, hardness, and magnetic properties in Fe58Cr27Co15 samples led us to conclude that:

(1) Lattice constant increased as step aging progressed.

(2) In certain sample that was annealed at 645 °C for only 10 min, spinodal decomposition had already occurred. In other samples that were annealed longer than 10 min at various temperatures, the size of the $\alpha_1$ phase increased as step aging progressed. The volume fraction of the $\alpha_1$ phase increased significantly during the early stages of spinodal decomposition and then maintained that level during the later stages.

(3) The $\alpha_1$ phase was rich in both Co and Fe, whereas the $\alpha_2$ phase was rich in Cr. In both $\alpha_1$ and $\alpha_2$ phases, the degree of enrichment of the dominant elements of both phases increased steadily as step aging progressed. During the last step, however, that trend changed. In the $\alpha_1$ phase, for example, Co content decreased and in the $\alpha_2$ phase, Cr decreased.

(4) After the first six steps of aging, the wavelength gradually increased as step aging progressed, which should have caused a decrease in hardness but did not do so because, at the same time, both wave amplitude and lattice misfit increased, thereby leading to an overall increase in hardness. In the last stage, decreases in both wave amplitude and lattice misfit led to a corresponding decrease in hardness.

(5) During the early stages of spinodal decomposition, both remanence and coercivity increased because of the increasing fluctuation of composition in both phases and the increasing volume of the $\alpha_1$ phase. As step aging progressed, the $\alpha_1$ phase stopped increasing in volume. Meanwhile, the $\alpha_1$ phase also coarsened, which should have decreased magnetic properties, but since the degree of fluctuation of composition continued to increase, leading to an overall increase in remanence and coercivity. In the last step, the degree of fluctuation of composition decreased, leading to a decrease in remanence.

(6) Comparison of changes in hardness, magnetic properties, and composition indicated that the relative fluctuation of composition between the $\alpha_1$ and $\alpha_2$ phases during step aging played a leading role in determining the hardness and the magnetic properties of FeCrCo alloys.

## Declaration of Competing Interest

The authors declare that they have no known competing financial interests or personal relationships that could have appeared to influence the work reported in this paper.

## Data availability

Data will be made available on request.

## Acknowledgement

This work was supported by the National Natural Science Foundation of China (51674083 and No. U1760206) and the 111 Project (2.0) of China (BP0719037). A portion of this work was performed at the National High Magnetic Field Laboratory (NHMFL), which is supported by National Science Foundation (Cooperative Agreement No. DMR-1157490, DMR-2128556 and DMR-1644779) and the State of Florida. Zhaolong Xiang and Bailing An were supported by the China Scholarship Council (CSC). The authors thank Mary Tyler for editing.

## References

[1] H. Kaneko, M. Homma, K. Nakamura, M. Miura, Fe-Cr-Co permanent magnet alloys containing silicon, IEEE Trans. Magn. 8 (1972) 347–348.
[2] H. Kaneko, M. Homma, K. Nakamura, New ductile permanent magnet of Fe-Cr-Co system, AIP Conf. Proc. 5 (1972) 1088–1092.
[3] S. Jin, Deformation-induced anisotropic Cr-Co-Fe permanent magnet alloys, IEEE Trans. Magn. 15 (1979) 1748–1750.
[4] A. Hütten, G. Reiss, W. Saikaly, G. Thomas, Origin of giant magnetoresistance in conventional AlNiCo5 magnets, Acta Mater. 49 (2001) 827–835.
[5] L. Zhou, W. Guo, J.D. Poplawsky, L. Ke, W. Tang, I.E. Anderson, M.J. Kramer, On spinodal decomposition in alnico - a transmission electron microscopy and atom probe tomography study, Acta Mater. 153 (2018) 15–22.
[6] S.I. Stel'mashok, I.M. Milyaev, V.S. Yusupov, A.I. Milyaev, Magnetic and mechanical properties of hard magnetic alloys 30Kh21K3M and 30Kh20K2M2V, Met. Sci. Heat Treat. 58 (2017) 622–627.
[7] H. Zijlstra, Trends in permanent magnet material development, IEEE Trans. Magn. 14 (1978) 661–664.
[8] M. Altafi, E. Mohammad Sharifi, A. Ghasemi, The effect of various heat treatments on the magnetic behavior of the Fe-Cr-Co magnetically hard alloy, J. Magn. Magn. Mater. 507 (2020), 166837.
[9] R.A. Rastabi, A. Ghasemi, M. Tavoosi, M. Ramazani, Magnetic features of Fe-Cr-Co alloys with tailoring chromium content fabricated by spark plasma sintering, J. Magn. Magn. Mater. 426 (2017) 744–752.
[10] S. Tao, Z. Ahmad, P. Zhang, X. Zheng, F. Wang, X. Xu, Enhancement of magnetic and microstructural properties in Fe-Cr-Co-Mo-V-Zr-Y permanent magnetic alloy, J. Magn. Magn. Mater. 484 (2019) 88–94.
[11] B.O. Mukhamedov, A.V. Ponomareva, I.A. Abrikosov, Spinodal decomposition in ternary Fe-Cr-Co system, J. Alloys Compd. 695 (2017) 250–256.
[12] A.A. Shatsov, I.V. Ryaposov, V.A. Kozvonin, Concertation-inhomogeneous hard magnetic alloys of the Fe-Cr-Co system with elevated content of cobalt and boron, Met. Sci. Heat Treat. 59 (2017) 45–49.
[13] O.A. Ushakova, E.H. Dinislamova, M.V. Gorshenkov, D.G. Zhukov, Structure and magnetic properties of Fe-Cr-Co nanocrystalline alloys for permanent magnets, J. Alloys Compd. 586 (2014) S291–S293.
[14] J. Li, L. Liu, H. Sepehri-Amin, X. Tang, T. Ohkubo, N. Sakuma, T. Shoji, A. Kato, T. Schrefl, K. Hono, Coercivity and its thermal stability of Nd-Fe-B hot-deformed magnets enhanced by the eutectic grain boundary diffusion process, Acta Mater. 161 (2018) 171–181.
[15] X. Tang, H. Sepehri-Amin, M. Matsumoto, T. Ohkubo, K. Hono, Role of co on the magnetic properties of Ce-substituted Nd-Fe-B hot-deformed magnets, Acta Mater. 175 (2019) 1–10.
[16] Z. Wang, K. Pei, J. Zhang, R. Chen, W. Xia, J. Wang, M. Li, A. Yan, Correlation between the microstructure and magnetic configuration in coarse-grain inhibited hot-deformed Nd-Fe-B magnets, Acta Mater. 167 (2019) 103–111.
[17] S. Tao, Z. Ahmad, I.U. Khan, P. Zhang, X. Zheng, Phase, microstructure and magnetic properties of 45.5Fe-28Cr-20Co-3Mo-1.5Ti-2Nb permanent magnet, J. Magn. Magn. Mater. 469 (2019) 342–348.
[18] D. Wang, N. Poudyal, C. Rong, Y. Zhang, M.J. Kramer, J. Ping Liu, Exchange-coupled nanoscale SmCo/NdFeB hybrid magnets, J. Magn. Magn. Mater. 324 (2012) 2836–2839.
[19] Q. Wang, L. Zheng, S. An, T. Zhang, C. Jiang, Thermal stability of surface modified Sm2Co17-type high temperature magnets, J. Magn. Magn. Mater. 331 (2013) 245–249.
[20] Z. Ahmad, A. Ul Haq, M. Yan, Z. Iqbal, Evolution of phase, texture, microstructure and magnetic properties of Fe-Cr-Co-Mo-Ti permanent magnets, J. Magn. Magn. Mater. 324 (2012) 2355–2359.

[21] H. Kaneko, M. Homma, T. Minowa, Effect of V and V + Ti additions on the structure and properties of Fe-Cr-Co ductile magnet alloys, IEEE Trans. Magn. 12 (1976) 977–979.

[22] H. Kaneko, M. Homma, T. Fukunaga, M. Okada, Fe-Cr-Co permanent magnet alloys containing Nd and Al, IEEE Trans. Magn. 44 (1975) 1–6.

[23] H. Kaneko, M. Homma, K. Nakamura, Phase diagram of Fe-Cr-Co permanent magnet system, IEEE Trans. Magn. 13 (1977) 1325–1327.

[24] T. Nishizawa, M. Hasebe, M. Ko, Thermodynamic analysis of solubility and miscibility gap in ferromagnetic alpha iron alloys, Acta Metall. 27 (1979) 817–828.

[25] T. Minowa, M. Okada, M. Homma, Further studies of the miscibility gap in an Fe-Cr-Co permanent magnet system, IEEE Trans. Magn. 16 (1980) 529–533.

[26] S. Jin, S. Mahajan, D. Brasen, Mechanical properties of Fe-Cr-Co ductile permanent magnet alloys, Metall. Mater. Trans. A. 11 (1980) 69–76.

[27] T.S. Chin, T.S. Wu, C.Y. Chang, T.K. Hsu, Y.H. Chang, Electron microscopy and magnetic properties of Fe-Cr-Co-Si permanent magnet alloys manufactured by rolling-ageing technique, J. Mater. Sci. 18 (1983) 1681–1688.

[28] X.Y. Sun, C.Y. Xu, L. Zhen, L.X. Lv, L. Yang, Evolution of modulated structure in Fe-Cr-Co alloy during isothermal ageing with different external magnetic field conditions, J. Magn. Magn. Mater. 312 (2007) 342–346.

[29] X.Y. Sun, C.Y. Xu, L. Zhen, L.X. Lu, L.C. Qin, Spinodal decomposition in Fe-25Cr-12Co-1Si alloy under a 100 kOe magnetic field, J. Magn. Magn. Mater. 306 (2006) 69–72.

[30] H. Kaneko, M. Homma, M. Okada, S. Nakamura, N. Ikuta, Fe-Cr-Co ductile magnet with (BH)max=8 MGOe, AIP Conf. Proc. 620 (1976) 620–621.

[31] S. Jin, N.V. Gayle, Low-cobalt Cr-Co-Fe magnet alloys obtained by slow cooling under magnetic field, IEEE Trans. Magn. 16 (1980) 526–529.

[32] M. Okada, R. Togashi, S. Sugimoto, M. Homma, Radially induced magnetic anisotropy in Fe-Cr-Co permanent magnets, J. Appl. Phys. 64 (1988) 5732–5734.

[33] Z. Ahmad, A. Ul Haq, S.W. Husain, T. Abbas, Magnetic properties of isotropic Fe-28Cr-15Co-3.5Mo permanent magnets with additives, Phys. B Condens. Matter 321 (2002) 54–59.

[34] B.A. Samarin, A.E. Kolchin, Y.V. Kal'Ner, Effect of prior aging and flat rooling on the structure and magnetic properties of alloys of the Fe-Cr-Co-Cu system, Met. Sci. Heat Treat. 28 (1986) 690–693.

[35] S. Sugimoto, M. Okada, M. Homma, The enhancement of the magnetic properties of Fe-Cr-Co-Mo polycrystalline permanent magnet alloys by cold rolling and annealing, J. Appl. Phys. 63 (1988) 3707–3709.

[36] T.S. Chin, T.H. Chen, C.Y. Chen, Magnetic properties and microstructures of Fe-Cr-10wt%Co-M (M= Si/Ti/Ni/Mo/Ge/ta) permanent magnet alloys, J. Magn. Magn. Mater. 50 (1985) 214–222.

[37] L. Yang, X.Y. Sun, L. Zhen, Y.B. Zhang, Hyperfine structure variations in an Fe-Cr-Co alloy exposed to electron irradiation: Mössbauer spectroscopy characterization, Nucl. Instrum. Methods Phys. Res. Sect. B. 338 (2014) 52–55.

[38] V.V. Serikov, N.M. Kleinerman, A.V. Vershinin, E.V. Beloserov, N.V. Mushnikov, G. V. Ivanova, N.N. Shchegoleva, M.A. Uimin, Effect of alloying elements on the structure peculiarities and mechanical properties of high-strength magnetic Fe-Cr-Co based alloys, Solid State Phenom. 168–169 (2011) 388–391.

[39] E.V. Belozerov, N.V. Mushnikov, G.V. Ivanova, N.N. Shchegoleva, V.V. Serikov, N. M. Kleinerman, A.V. Vershinin, M.A. Uimin, High-strength magnetically hard Fe-Cr-Co-based alloys with reduced content of chromium and cobalt, Phys. Met. Metallogr. 113 (2012) 319–325.

[40] Z. Xiang, L. Zhang, Y. Xin, B. An, R. Niu, M. Mardani, T. Siegrist, J. Lu, R. E. Goddard, T. Man, E. Wang, K. Han, Ultrafine microstructure and hardness in Fe-Cr-Co alloy induced by spinodal decomposition under magnetic field, Mater. Des. 199 (2021), 109383.

[41] S. Sugimoto, M. Okada, M. Homma, H. Satoh, Evolution process of ⟨100⟩ texture in Fe-Cr-Co-Mo permanent magnets, Mater. Trans. 32 (1991) 557–561.

[42] A. Takahashi, T. Suzuki, A. Nomoto, T. Kumagai, Influence of spinodal decomposition structures on the strength of Fe-Cr alloys: a dislocation dynamics study, Acta Mater. 146 (2018) 160–170.

[43] K.H. Park, J.C. LaSalle, L.H. Schwartz, M. Kato, Mechanical properties of spinodally decomposed Fe-30 wt% Cr alloys: yield strength and aging embrittlement, Acta Metall. 34 (1986) 1853–1865.

[44] Y. Xin, K. Han, Z. Liang, Y.F. Su, P.J. Lee, D.C. Larbalestier, Aberration-corrected S/TEM at Florida State University, Microsc. Today 22 (2014) 42–49.

[45] Y. Xin, J. Kynoch, K. Han, Z.Y. Liang, P.J. Lee, D.C. Larbalestier, Y.F. Su, K. Nagahata, T. Aoki, P. Longo, Facility implementation and comparative performance evaluation of probe-corrected TEM/STEM with schottky and cold field emission illumination, Microsc. Microanal. 19 (2013) 487–495.

[46] K. Han, K.Y. Zhang, Transmission electron microscopy study of metallic multilayers, Scr. Mater. 50 (2004) 781–786.

[47] L.X. Lv, L. Zhen, C.Y. Xu, X.Y. Sun, Phase field simulation of microstructure evolution in Fe-Cr-Co alloy during thermal magnetic treatment and step aging, J. Magn. Magn. Mater. 322 (2010) 987–995.

[48] K. Han, M.J. Van Genderen, A. Bottger, H.W. Zandbergen, E.J. Mittemeijer, Initial stages of Fe-C martensite decomposition, Philos. Mag. A. 81 (2001) 741–757.

[49] S.I. Kondo, T. Morimura, H. Nakashima, A. Masusaki, K. Ogawa, Effects of initial states on the spinodal decomposition of quenched and melt-spun Cu-15Ni-8Sn alloy, Mater. Trans. 79 (2015) 664–671.

[50] J.C. Zhao, M.R. Notis, Spinodal decomposition, ordering transformation, and discontinuous precipitation in a Cu-15Ni-8Sn alloy, Acta Mater. 46 (1998) 4203–4218.

[51] C.K. Wu, G. Thomas, Microstructure and properties of a Cu-Ni-Cr spinodal alloy, Metall. Trans. A. 8 (1977) 1911–1916.

[52] Y. Xin, Q. Huang, Z. Shafieizadeh, H. Zhou, B-site cation order/disorder and their valence states in $Ba_3MnNb_2O_9$ perovskite oxide, J. Solid State Chem. 262 (2018) 8–15.

[53] S.J. Pennycook, L.A. Boatner, Chemically sensitive structure-imaging with a scanning transmission electron microscope, Nat. Publ. Gr. 336 (1988) 565–567.

[54] F. Findik, H.M. Flower, Microstructure and hardness development in Cu-30Ni-25Cr and Cu-45Ni-10Cr spinodal alloys, Mater. Sci. Technol. 8 (1992) 197–205.

[55] O. Soriano-Vargas, E.O. Avila-Davila, V.M. Lopez-Hirata, N. Cayetano-Castro, J. L. Gonzalez-Velazquez, Effect of spinodal decomposition on the mechanical behavior of Fe-Cr alloys, Mater. Sci. Eng. A 527 (2010) 2910–2914.

[56] K.V. Shankar, R. Sellamuthu, Determination on the effect of tin content on microstructure, hardness, optimum aging temperature and aging time for spinodal bronze alloys cast in metal mold, Int. J. Met. 11 (2017) 189–194.

[57] F. Danoix, P. Auger, D. Blavette, Hardening of aged duplex stainless steels by spinodal decomposition, Microsc. Microanal. 10 (2004) 349–354.

[58] J.W. Chan, Harding by spinodal decomposition, Acta Metall. 11 (1963) 1275–1282.

[59] L.H. Schwartz, S. Mahajan, J.T. Plewes, Spinodal decomposition in a Cu-9wt%Ni-6wt%Sn alloy, Acta Metall. 22 (1974) 601–609.

[60] A. Chou, A. Datta, G.H. Meier, W.A. Soffa, Microstructural behavior and mechanical hardening in a Cu-Ni-Cr alloy, J. Mater. Sci. 13 (1978) 541–552.

[61] M. Kato, Harding by spinodally modulated structure in bcc alloys, Acta Metall. 29 (1981) 79–87.

[62] R. Wagner, Hardening in spinodal decomposition alloys, J. Phys. B. 31 (1981) 198–208.

[63] W. Tang, Y.Q. Wu, K.W. Dennis, M.J. Kramer, I.E. Anderson, R.W. McCallum, Effect of TiC addition on microstructure and magnetic properties for $MRE_2(Fe,Co)_{14}B$ melt-spun ribbons (MRE=Nd+Y+Dy), J. Appl. Phys. 99 (2006) 1–4.

[64] T. Zhang, W. Xing, F. Chen, S. Liu, L. Zhang, R. Yu, Microstructure and phase evolution mechanism in hot-pressed and hot-deformed Nd-Fe-B magnets with $Nd_{85}Cu_{15}$ addition, Acta Mater. 204 (2021), 116493.

[65] O. Gutfleisch, K.H. Müller, K. Khlopkov, M. Wolf, A. Yan, R. Schäfer, T. Gemming, L. Schultz, Evolution of magnetic domain structures and coercivity in high-performance SmCo 2:17-type permanent magnets, Acta Mater. 54 (2006) 997–1008.

[66] A.K. Pathak, M. Khan, K.A. Gschneidner, R.W. McCallum, L. Zhou, K. Sun, M. J. Kramer, V.K. Pecharsky, Magnetic properties of bulk, and rapidly solidified nanostructured $(Nd_{1\text{-}x}Ce_x)_2Fe_{14\text{-}y}Co_yB$ ribbons, Acta Mater. 103 (2016) 211–216.

[67] A.K. Pathak, M. Khan, K.A. Gschneidner, R.W. McCallum, L. Zhou, K. Sun, K. W. Dennis, C. Zhou, F.E. Pinkerton, M.J. Kramer, V.K. Pecharsky, Cerium: an unlikely replacement of dysprosium in high performance Nd-Fe-B permanent magnets, Adv. Mater. 27 (2015) 2663–2667.

[68] M. Homma, E. Horikoshi, T. Minowa, M. Okada, High-energy Fe-Cr-Co permanent magnets with (BH)max ≃8-10 MG Oe, Appl. Phys. Lett. 37 (1980) 92–93.

[69] W.C. Chang, S.H. Wu, B.M. Ma, C.O. Bounds, S.Y. Yao, Magnetic properties enhancement of α-$Fe/Nd_2Fe\ _{14}B$-type nanocomposites by Co substitution, J. Appl. Phys. 83 (1998) 2147–2151.

[70] E.C. Stoner, E.P. Wohlfarth, A mechanism of magnetic hysteresis in heterogeneous alloys, Math. Phys. Sci. 240 (1948) 599–642.

[71] S. Drápal, The origin of anisotropy in Fe-Cr-Co alloys, Czech. J. Phys. B 37 (1987) 1174–1182.

[72] A. López-Ortega, M. Estrader, G. Salazar-Alvarez, A.G. Roca, J. Nogués, Applications of exchange coupled bi-magnetic hard/soft and soft/hard magnetic core/shell nanoparticles, Phys. Rep. 553 (2015) 1–32.

[73] A.S. Bolyachkin, A.S. Volegov, N.V. Kudrevatykh, Intergrain exchange interaction estimation from the remanence magnetization analysis, J. Magn. Magn. Mater. 378 (2015) 362–366.

[74] A. Xia, Y. Li, T. Li, S. Su, C. Jin, X. Liu, The availability of Henkel plots for sintered hard/soft magnetic composite ferrites, Phys. B 493 (2016) 14–16.